Journal of Alloys and Compounds 947 (2023) 169630

Contents lists available at ScienceDirect

Journal of Alloys and Compounds

journal homepage: www.elsevier.com/locate/jalcom

Flash joule heating synthesis of carbon supported ultrafine metallic heterostructures for high-performance overall water splitting

Ping Li [a], Wenjie Wei [a], Jin Li [a], Yanru Liu [a], Kaicai Fan [b,*], Lingbo Zong [a,*], Lei Wang [a]

[a] College of Chemistry and Molecular Engineering, Qingdao University of Science and Technology, Qingdao 266042, China
[b] College of Materials Science and Engineering, Qingdao University of Science and Technology, Qingdao 266042, China

ARTICLE INFO

Article history:
Received 12 December 2022
Received in revised form 7 March 2023
Accepted 9 March 2023
Available online 11 March 2023

Keywords:
Flash joule heating
Ultrafine metallic heterostructures
Hydrogen evolution reaction
Oxygen evolution reaction
Overall water splitting

ABSTRACT

Hydrogen evolution reaction (HER) and oxygen evolution reaction (OER) are pivotal electrochemical reactions in water splitting and require efficient and durable electrocatalysts. Developing carbon-supported ultrafine nanocrystals embracing rich active sites serves an effective strategy to produce efficient electrocatalysts. Herein, we report a facile flash joule heating technology to prepare bifunctional electrocatalyst toward HER and OER, in which ultrafine Cu and Ru metallic heterostructures confined within carbon matrix are directly coated on the conductive carbon cloth (Ru-Cu@CM/CC). Benefiting from the homogeneously dispersed nanoclusters with rich active sites, Ru-Cu@CM/CC shows remarkable performance for HER and OER in both alkaline and acid solution, outperforming Pt/C and RuO_2, respectively. Remarkably, the two-electrode electrolyzers using Ru-Cu@CM/CC display low voltages in alkaline and acid electrolyte. The exemplified Ru-Cu@CM/CC illustrates the effectiveness of flash joule heating strategy in preparing metallic heterostructures. The satisfactory electrocatalytic performance also inspires the construction of heterostructures for overall water splitting.

1. Introduction

Hydrogen, as clean and sustainable energy carrier, has been emerged as the best answer for the increasingly serious energy crisis and environment problems [1–4]. Electrochemical water electrolysis is a clean, sustainable and effective way to produce hydrogen without any carbon footprint. Hydrogen evolution reaction (HER) and oxygen evolution reaction (OER) occurred on the cathode and anode of electrolyzer are of central importance in water electrolysis [5–8]. Nevertheless, practical application of water electrolysis is significantly hampered by sluggish kinetics of HER and OER, which induce large energy loss of the electrolyzer [9–11]. Therefore, developing efficient electrocatalysts for HER and OER is desirable and in urgent need. Specifically, bifunctional electrocatalysts, which are capable of catalyzing HER and OER effectively with low overpotentials, are of great importance as the bifunctional electrocatalysts inherit the merits of simplifying the fabrication procedure and reducing the price of electrolyzer [7,12–18]. Thus, exploring rational strategy to produce efficient bifunctional catalysts for HER and OER is fascinating for the practical application of electrolyzer.

Ultrafine nanoparticles with rich accessible active sites and excellent electrocatalytic performance have been investigated as potential electrocatalysts.[19–23] Despite the great progress in preparing those well-dispersed nanoparticles, it still faces some hurdles to be surmounted eagerly. Firstly, ultrafine nanoparticles are easy to agglomerate into the large ones during the long-term testing [24]. Secondly, nanoparticles suffer from dissolution under harsh acidic solutions. Recently, supporting the ultrafine nanoparticles onto the carbon matrix deserves special attention to impede the agglomeration and dissolution of nanoparticles [25]. Amongst, as a classic and promising porous crystalline material, MOFs with high surface area can be converted to the metal nanoparticles confined in carbon shell, and are thus under intensive investigations and are promising to obtain bifunctional electrocatalysts [26–29]. Furthermore, the electrocatalytic reactions always involve the adsorption and desorption of the reaction intermediates, and the bindings of those intermediates determine the electrocatalytic activity.[30–34] In this regard, heterostructures are built to modulate the binding energies of those intermediates and have been demonstrated to be applicable to enhance electrocatalytic activity towards various reactions including HER and OER [35–37]. For instance, Ru species typically show satisfactory water dissociation kinetics in alkaline

* Corresponding authors.
E-mail addresses: kaicai.fan@outlook.com (K. Fan), lingbozong@qust.edu.cn (L. Zong).

https://doi.org/10.1016/j.jallcom.2023.169630
0925-8388/

solution and are intensively used as excellent electrocatalysts for water splitting [38]. However, the binding of H atoms on Ru is too strong, and the desorption of H atoms hinders the enhancement of catalytic performance. Considering the weak Cu-H interaction between Cu and H, integrating Ru and Cu is proposed to facilitate the adsorption of reaction intermediates and enhance both HER and OER [39,40]. Thus, exploring facile strategy to construct rational heterostructure is challenging and rewarding. Additionally, in the typical electrocatalysts ink preparation procedure, the electrocatalysts with powder form that are directly loaded on the surface of glassy carbon electrode or conductive substrates can be easily peeled off from the working electrodes [23]. Also, the application of nonconductive polymer binders can impede the charge transport and impair the catalytic properties [23,41]. Therefore, rational strategy to fabricate the bifunctional electrocatalyst, in which carbon supported ultrafine heterostructure nanocrystals are immobilized on conductive substrates, is particularly auspicious to obtain efficient and durable electrolyzer for overall water splitting.

Here, we offer an exciting flash joule heating strategy to fabricate carbon-coated ultrafine metallic heterostructures of Cu and Ru nanocrystals on the conductive carbon cloth (Ru-Cu@CM/CC). During the flash joule heating process, the Cu species in Cu-MOFs are carbothermal reduced to metallic Cu nanocrystals, which are simultaneously encapsulated by the MOFs-derived carbon with the originally embedded Ru nanocrystals. The heterostructures embracing Cu and Ru nanocrystals with sterling dispersion inside carbon matrix give rise to the enhanced utilization of active sites. Notably, metallic heterostructures are also expected to optimize the adsorption and desorption behavior of intermediates, and render satisfactory electrocatalytic activity. Thus, Ru-Cu@CM/CC displays small overpotentials for HER and OER in 1.0 M KOH and 0.5 M H_2SO_4 electrolyte. The electrolyser using Ru-Cu@CM/CC needs low cell voltages of only 1.57 V and 1.60 V to deliver 10 mA cm^{-2} in alkaline and acidic electrolytes, respectively. The exemplified flash joule heating strategy holds great promises in producing prudent metallic heterostructures, which can be used to efficiently catalyze other electrocatalytic reaction, such as oxygen reduction reaction and carbon dioxide reduction.

2. Experimental Section

2.1. Materials

Copper acetate ($Cu(CH_3COO)_2$), 1,3,5-Benzenetricarboxylic acid ($C_9H_6O_6$), ruthenium chloride ($RuCl_3$), and ethanol (C_2H_5OH) were obtained from Sinopharm Chemical Reagent Co., Ltd.

2.2. Synthesis of Ru-Cu@CM/CC electrocatalyst

The carbon cloth was soaked in ethanol solution containing 1.0 mM 1,3,5-Benzenetricarboxylic acid for 40 min. After that it was placed in ethanol solution containing 1.0 mM copper acetate for 20 min. Carbon cloth with repeating four times of above steps was dried at 50 °C for 6 h. The obtained sample was then put into the Teflon lined autoclave containing the mixed solution of 1,3,5-Benzenetricarboxylic acid, $Cu(NO_3)_2$ (7.5 mL, 0.05 M) and $RuCl_3$ (7.5 mL, 0.01 M), and the reactor was heated in the oven for 12 h at 150 °C. Afterwards, the obtained products was pyrolyzed in a Joule furnace under the protection of nitrogen at 1000 °C for only 0.5 s, to yield Ru-Cu@CM/CC.

2.3. Synthesis of Cu@CM/CC reference

Cu@CM/CC was fabricated by using the similar synthetic method without the addition of $RuCl_3$.

2.4. Characterizations

X-ray diffraction (XRD) patterns and X-ray photoelectron spectroscopy (XPS) spectra were tested by Philips PANalytical X′Pert Pro with Cu Kα radiation (λ = 1.5418 Å) and ESCALab MKII XPS system, respectively. Metal contents of as-developed Ru-Cu@CM/CC were measured by inductively coupled plasma mass spectrometry (ICP-MS, Thermo iCAP RQ). Scanning electron microscope (SEM), and transmission electron microscopy (TEM) were conducted on Zeiss sigma 500, and JEOL-2100 to detect the morphology and energy-dispersive X-ray spectroscopy (EDX) mapping, respectively.

2.5. Electrochemical characterization

Hydrogen evolution reaction (HER) and oxygen evolution reaction (OER) measurements were conducted in a three-electrode electrochemical cell at room temperature. The as-developed samples were served as working electrode. 1.0 M KOH and 0.5 M H_2SO_4 were served as the electrolytes to evaluate HER and OER activities. For the electrochemical test in 1.0 M KOH, Hg/HgO electrode was used as reference electrode, and graphite rod was applied as counter electrode. In 0.5 M H_2SO_4, Ag/AgCl reference electrode and graphite rod were served as reference electrode and counter electrode, respectively. For the Pt/C or RuO_2 electrocatalyst ink, 5 mg of Pt/C or RuO_2 was dispersed in a mixed solution of 720.0 μL isopropyl alcohol, 240.0 μL deionized water, and 40.0 μL Nafion solution. The electrocatalyst loading capacity for Pt/C or RuO_2 benchmarks was 0.255 mg cm^{-2}. The stability of as-developed electrocatalyst were evaluated by the accelerated degradation test and current density (*j*)-time (t) chronoamperometric response. All the obtained electrode potentials were calibrated to reversible hydrogen electrode (RHE) with 95% *i*R compensation.

3. Results and discussion

Typically, the size and composition of bimetal nanoclusters show significant influence in the electronic structures, which determines the electrocatalytic performance for HER and OER. Thus, unique heterostructures of metallic Ru and Cu embedded in carbon matrix was prepared on carbon cloth (Ru-Cu@CM/CC) by a facile two-step process as illustrated by Scheme 1. Firstly, Cu-MOFs supported Ru nanocrystals was fabricated on a conductive carbon cloth (Ru@Cu-MOFs/CC) by a solvothermal approach using $Cu(NO_3)_2{\cdot}6\ H_2O$ as metal precursor and benzene tricarboxylic acid as the organic ligand. Secondly, Ru@Cu-MOFs/CC was carbothermal reduced by the flash joule heating strategy under N_2 atmosphere. The ultrahigh temperature can drive the “fission” and “fusion” for Cu and Ru species and form uniform mixtures of both elements. Then, by controlling the rapid cooling process, phase-separated CuRu heterostructures were obtained.[42] Finally, metallic Cu was generated and MOFs skeleton was carbonized to form conductive carbon matrix. Together with the originally supported Ru nanocrystals, heterostructure Ru and Cu nanocrystals in carbon matrix (Ru-Cu@CM/CC) were obtained after flash joule heating.

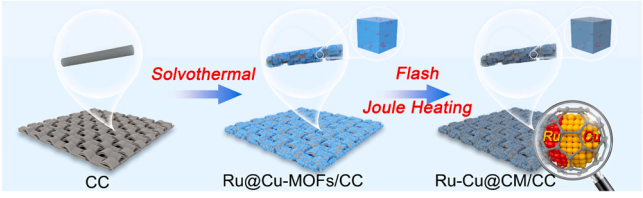

Scheme 1. Schematic illustration for the synthesis of Ru-Cu@CM/CC.

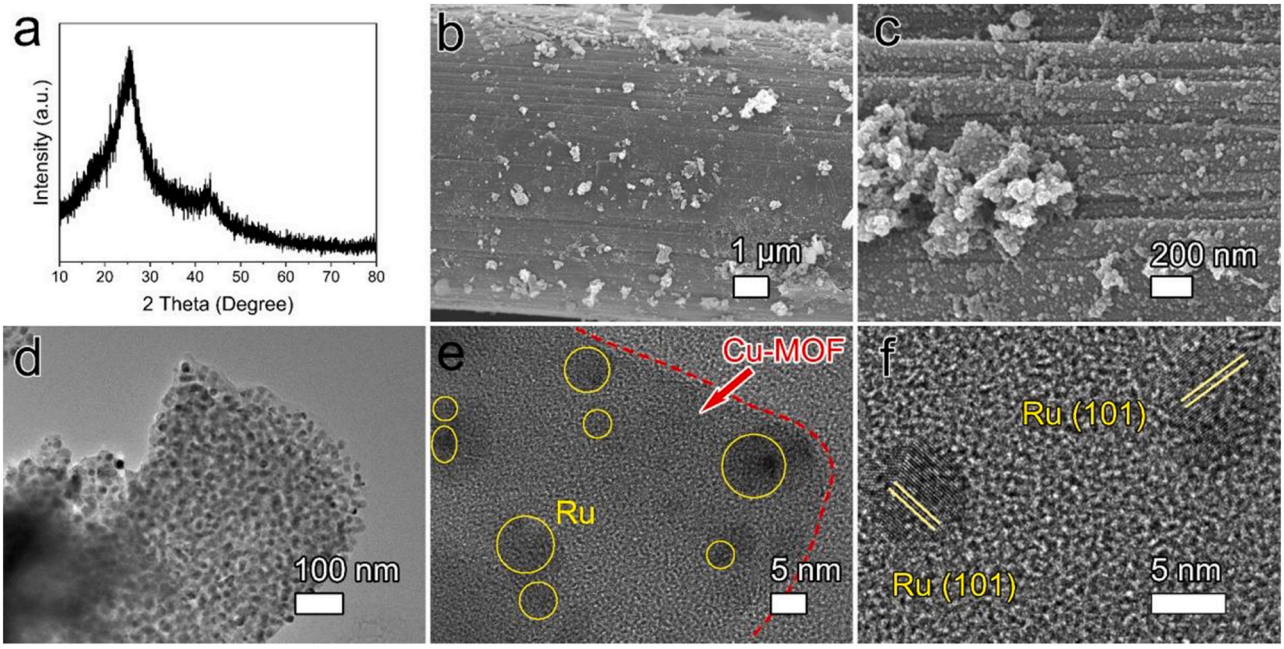

Fig. 1. (a) XRD pattern of Ru@Cu-MOFs/CC. (b, c) SEM images of Ru@Cu-MOFs/CC. (d) TEM image of Ru@Cu-MOFs/CC and (e) corresponding size distribution of the supported Ru nanocrystals. (f) HR-TEM image of Ru@Cu-MOFs/CC.

X-ray diffraction (XRD), scanning electron microscopy (SEM), and transmission electron microscopy (TEM) were applied to characterize the structure of Ru@Cu-MOFs/CC. XRD pattern (Fig. 1a) displays that the diffraction peaks at 25.0° and 43.1° are assigned to the crystalline planes of carbon cloth. Similar to the XRD pattern of the pure Cu-MOFs/CC (Fig. S1), the diffraction peaks assigning to Cu-MOFs cannot be observed, ambiguously revealing the formation of low-crystalized MOFs. SEM and TEM were then conducted to detect the morphology and spatial position of Cu-MOFs and Ru nanocrystals in Ru@Cu-MOFs/CC. The representative SEM images of Ru@Cu-MOFs/CC show well-defined small Ru@Cu-MOFs nanoparticles, which are uniformly coated on carbon cloth, though a certain number of aggregated nanoparticles are observed. (Figs. 1b, 1c, and Fig. S2). Notably, Cu-MOFs/CC possess an analogous morphology as Ru@Cu-MOFs, demonstrating that the introduction of Ru element did not affect the growth of Cu-MOFs (Fig. S3). TEM image of Ru@Cu-MOFs/CC (Fig. 1d) reaffirms that it is the assembly of small Cu-MOFs on the surface of carbon cloth. Fig. 1e further reveals that there are well-dispersed Ru nanoparticles supported in the Cu-MOFs without aggregation. As shown in Fig. S4, the average particle size of Ru nanocrystals is approximately 5.28 nm with encouraging crystallinity. The high-resolution TEM (HR-TEM) in Fig. 1f exhibits lattice fringes with distance of 2.05 Å, which is the (101) plane of metallic Ru. Thus, the Ru cations were reduced by the ethanol in the solution and metallic Ru nanocrystals formed during solvothermal process. In contrast, there is no nanocrystals can be distinguished in pure Cu-MOFs (Fig. S5), which reveal that Ru nanocrystals are successfully embedded in Cu-MOFs for Ru@Cu-MOFs/CC. The above results demonstrate that Ru species transformed into ultrafine metallic Ru nanocrystals and uniformly embed in the simultaneously generated small Cu-MOFs nanoparticles during the solvothermal reaction process.

To determine the surface chemical composition of Ru@Cu-MOFs/CC, X-ray photoelectron spectroscopy (XPS) was performed. From the XPS survey image of Ru@Cu-MOFs/CC, peaks assigned to Cu, O, Ru, and C signals can be obviously distinguished (Fig. S6), supporting the formation of composite. The O1s is attributed to the terephthalic acid, which is the organic ligand of Cu-MOFs. The high-resolution Ru 3*p* and Cu 2*p* XPS spectra were then carefully analyzed to identify the chemical state of both elements in Ru@Cu-MOFs/CC. For the Ru 3*p* XPS spectrum (Fig. S7), the main peaks at 485.0 eV and 462.6 eV are indexed to the $3p_{3/2}$ and $3p_{1/2}$ peak for oxidized Ru [43,44]. It should be noted that the XPS is a surface-sensitive technique. Therefore, oxidized Ru atoms on the surface of metallic nanocrystals are proposed to be coordinated with O atoms of Cu-MOFs, and the transfer of electrons from Ru to Cu-MOFs support contributes to the positive shift of binding energy comparing to metallic Ru [45]. Additionally, the Cu $2p_{1/2}$ peak at 954.8 eV, and Cu $2p_{3/2}$ peak at 934.9 eV are observed clearly (Fig. S8), illustrating the oxidation state of Cu is + 2 as pure Cu-MOFs/CC (Fig. S9) [46,47]. The above XPS analysis results reveal that metallic Ru nanocrystals are immobilized in Cu-MOFs via binding with the rich oxygen-containing functional groups in Cu-MOFs after the solvothermal process.

Ru@Cu-MOFs nanoparticles tightly coated on carbon cloth were then treated via the flash carbothermal reduction process for 0.5 s at 1000 °C in joule furnace under the protection of N_2 atmosphere. For comparison, Cu-MOFs/CC was also processed following the same procedures. XRD is performed to obtain the detailed information relating to the phase structure, and to investigate the conversion of Ru@Cu-MOFs/CC after the flash joule heating. Fig. 2a displays the XRD pattern of Ru-Cu@CM/CC, where the diffraction peaks at 43.3°, 50.5° and 74° demonstrate the existence of Cu nanocrystals. The representative diffraction peaks at 38.4°, 42.1°, 44° and 58.3° can be indexed to the metal Ru (PDF No. 06–0663). Therefore, the original crystallized Ru nanocrystals retained, and Cu species in Cu-MOFs were reduced to metallic Cu during the carbothermal reduction process. The morphological change during the flash joule heating process were then explored using SEM and TEM technique. As shown by the SEM images in Figs. 2b, 2c, Ru-Cu@CM/CC inherits the original morphology of Ru@Cu-MOFs/CC, which endows uniformly dispersed nanoparticles coated on carbon cloth. Thus, the flash joule heating strategy is effective to maintain the original morphology of the precursor, which is also evidenced by the SEM images of Cu@CM/CC (Fig. S10). Specifically, in shown Fig. 2c, those nanoparticles are well dispersed as Ru@Cu-MOFs/CC, indicating the morphological structure can be retained after flash joule heating. Furthermore, abundant highly dispersed Cu and Ru nanocrystals, which are confined within the carbon matrix, could be obviously discovered by

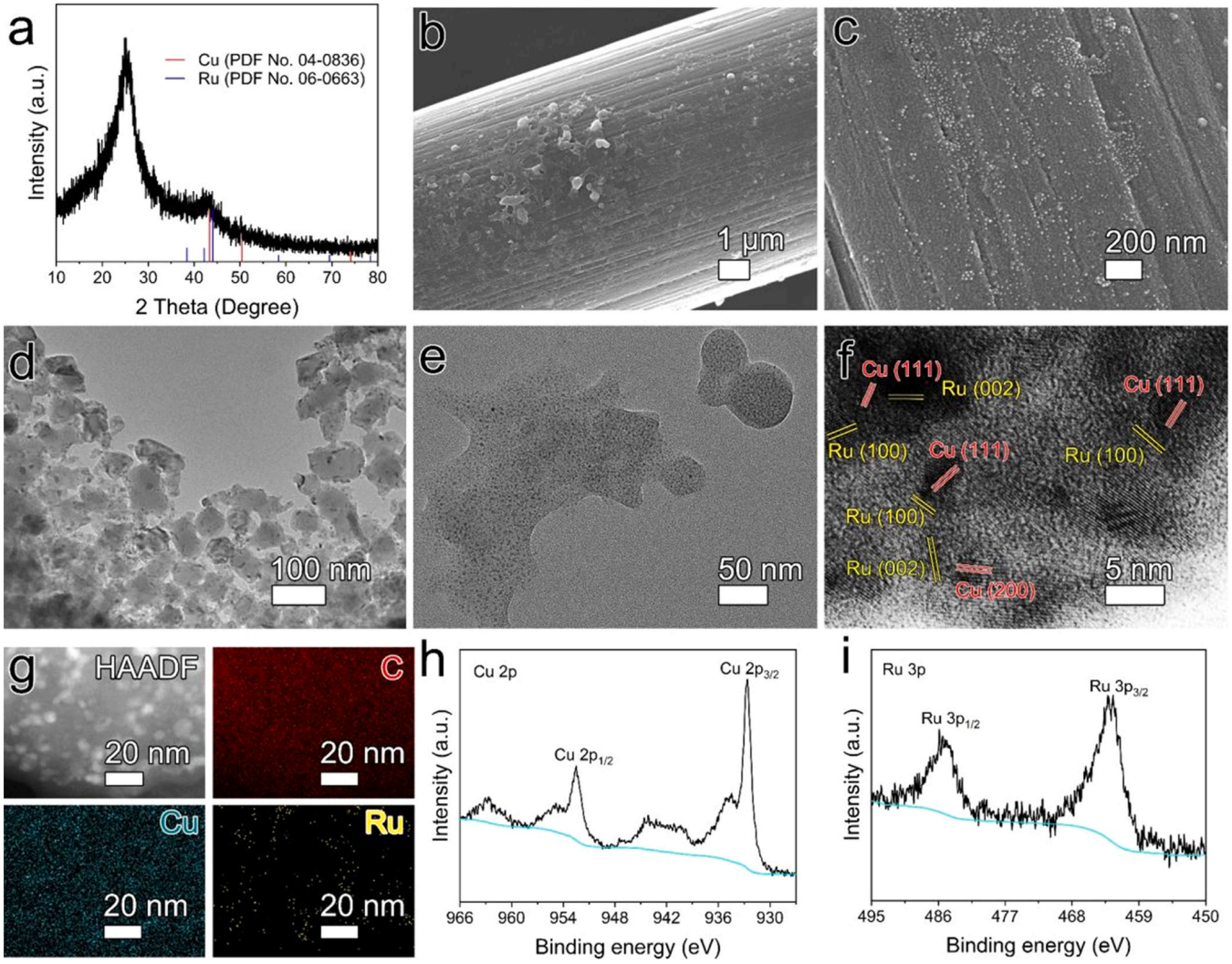

Fig. 2. (a) XRD pattern, (b, c) typical SEM images, (d-e) TEM images, and (f) HR-TEM image of Ru-Cu@CM/CC. (g) HAADF-STAM image and corresponding EDS mappings of Ru-Cu@CM/CC. High-resolution XPS spectra of Cu 2*p* (h), and Ru 3*p* (i) for Ru-Cu@CM/CC.

TEM image (Figs. 2d, 2e, and Fig. S11). The HR-TEM image displayed in Fig. 2f and Fig. S12 clearly exhibit that ultrafine Cu and Ru nanocrystals dispersed on carbon matrix show high crystallinity, and well-defined lattice fringes. The distinct interplanar distances can be well indexed to the crystallized Cu and Ru metals, consisting with above XRD result. Meanwhile, only uniformly dispersed metallic Cu nanocrystals can be observed in Cu@CM/CC (Fig. S13), supporting the conversion of Cu species into metallic Cu nanocrystals during the joule heating process. The high-angle annular dark-field scanning TEM (HAADF-STEM) further displays the highly dispersed Ru nanocrystals (Fig. 2g), as the brighter spots can be assigned to Ru and Cu elements with higher atomic numbers than C. The energy-dispersive spectroscopic (EDS) mappings render the existence of Cu and Ru elementals, demonstrating the retain of Cu and Ru nanocrystals by the flash joule heating approach through the rapid carbothermal reduction reaction. The above results demonstrate that the morphology of small nanoparticles is well inherited from the Cu-MOFs, and intimate interaction between those assembled nanoparticles and carbon cloth rendering a fast mass and electron transfer between reactant and conductive support, which could boost the electrocatalytic reaction. Notably, the well dispersed heterostructures generated during the joule flash heating process are expected to enhance the exposure of active species for electrocatalytic HER and OER.

The specific composition change during the flash joule heating process are then investigated using XPS. Cu 2*p* XPS spectrum can be divided into peaks at 952.5 eV and 932.6 eV, which are indexed to the metallic Cu (Fig. 2h) [46,48]. The above results demonstrate the reduction of Cu species in Cu-MOFs to metallic Cu nanocrystals after flash joule heating. In the Ru 3*p* XPS spectrum of Ru-Cu@CM/CC (Fig. 2i), the typical peaks presented at 483.4 eV and 461.4 eV are attributed to the metallic Ru [49]. Together with the originally embedded Ru nanocrystals, the metallic heterostructure are produced. The Ru and Cu contents over Ru-Cu@CM/CC is 0.024 wt%, and 1.811 wt%, respectively, based on inductively coupled plasma mass spectrometry (ICP-MS) analysis. The demonstrated heterostructure of Cu and Ru nanocrystals embedded in carbon matrix, which are firmly coated on carbon support, are expected to promote the adsorption/desorption of reaction intermediates and boost HER and OER activity.

Electrocatalytic performance towards HER of the electrocatalysts was firstly assessed in N_2 saturated 1.0 M KOH. Fig. 3a displays the linear sweep voltammetry (LSV) plots of HER for Ru-Cu@CM/CC, Cu@CM/CC, and Pt/C benchmark. Ru-Cu@CM/CC shows small overpotential in the potential range of 0–0.2 V comparing to Cu@CM/CC, Pt/C and other samples [50–52]. To achieve the current density of 10 mA cm^{-2} and 100 mA cm^{-2}, Ru-Cu@CM/CC requires the potential of only 25 mV and 94 mV, respectively, which are much smaller than

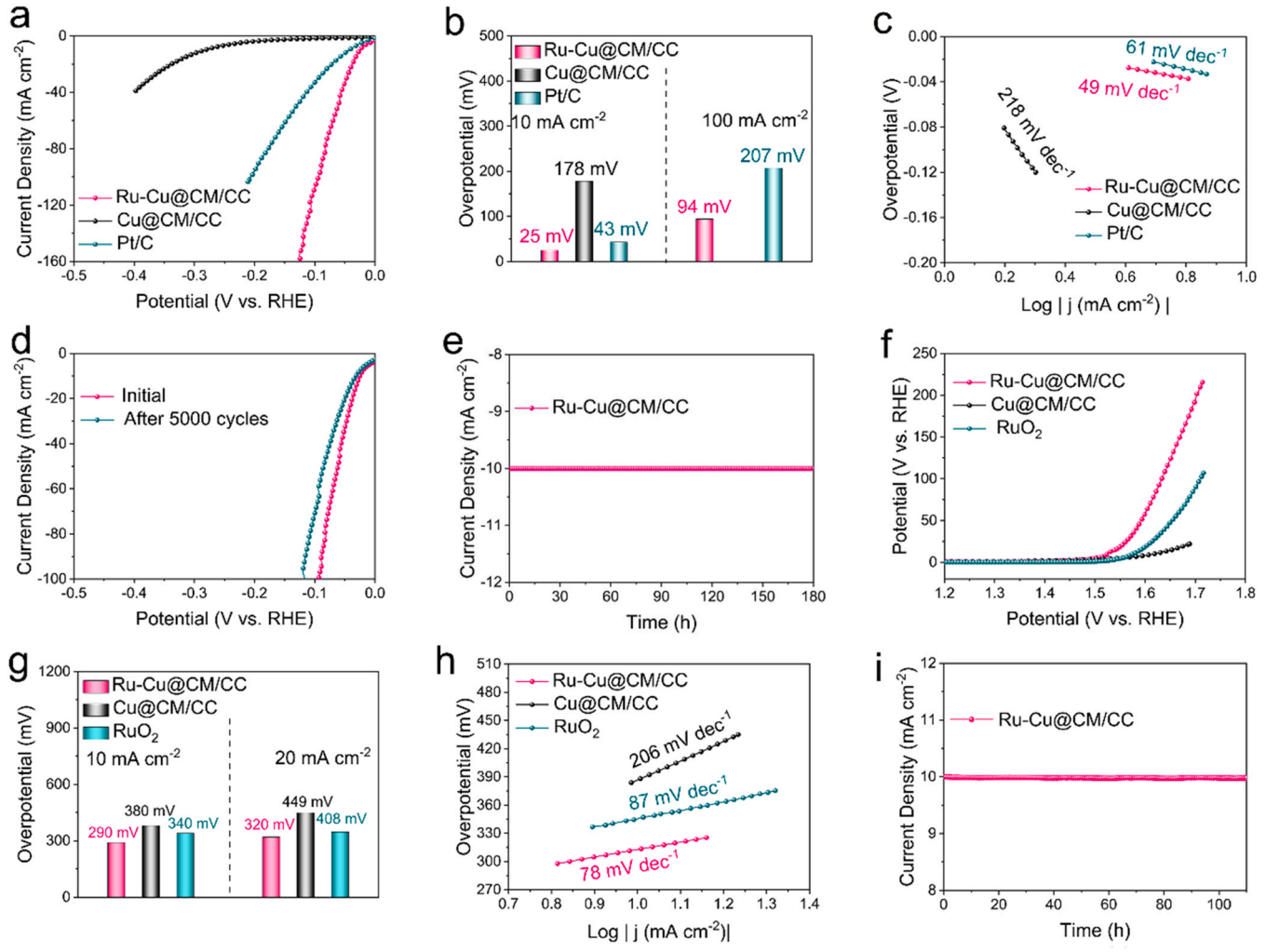

Fig. 3. (a) HER polarization curves for Ru-Cu@CM/CC, Cu@CM/CC, and Pt/C in 1.0 M KOH. (b) Comparison of overpotentials for Ru-Cu@CM/CC, Cu@CM/CC, and Pt/C at different current densities of 10 and 100 mA cm^{-2}. (c) The corresponding Tafel plots. (d) Polarization curves of Ru-Cu@CM/CC at the first cycle and after 5000 CV cycles. (e) Chronoamperometry test for Ru-Cu@CM/CC at − 25 mV. (f) OER polarization curves of Ru-Cu@CM/CC, Cu@CM/CC, and Pt/C in 1.0 M KOH. (g) Comparison of overpotentials for Ru-Cu@CM/CC, Cu@CM/CC, and RuO_2 at different current densities of 10 and 20 mA cm^{-2}. (h) The corresponding Tafel plots. (i) Chronoamperometry test for Ru-Cu@CM/CC at the potential of 290 mV.

that for Pt/C benchmark (Fig. 3b). This indicates that Ru-Cu@CM/CC is an excellent catalyst for HER, outperforming Pt/C benchmark. Tafel slope, the indicator of rate-limiting step, is analysed to evaluate the reaction kinetics [53]. As displayed by the Tafel plots in Fig. 3c, the Tafel slopes of Ru-Cu@CM/CC, Cu@CM/CC, and Pt/C benchmark are 49 mV dec^{-1}, 61 mV dec^{-1}, and 218 mV dec^{-1} respectively. In comparison with Ru-Cu@CM/CC, Cu@CM/CC yields a negligible HER activity. The electrical impedance spectroscopy (EIS) was conducted to study the charge-transfer resistance (R_{ct}) of Ru-Cu@CM/CC, Cu@CM/CC, and Pt/C benchmark, respectively. As shown in Fig. S14, the Rct value of Ru-Cu@CM/CC (5 Ω) is similar to that of Cu@CM/CC (7 Ω), and smaller than Pt/C benchmark (12 Ω). This is attributed to the fact that the direct growth of electrocatalysts shows better electrical contact to conductive carbon cloth than coating the electrocatalysts with polymer binders. Thus, the faster charge transfer rate of Ru-Cu@CM/CC contributes to better performance under high current density than Pt/C. Additionally, the electrochemically active surface areas (ECSAs), was measured by calculating the double layer capacitance values (C_{dl}). From the Fig. S15, it is determined that the C_{dl} value of Ru-Cu@CM/CC is 10.3 mF cm^{-2}, which is similar to those of Cu@CM/CC (7.3 mF cm^{-2}) and Pt/C benchmark (8.6 mF cm^{-2}), testifying the metallic heterostructures with high intrinsic electrocatalytic activity in Ru-Cu@CM/CC predominately contributed to the enhanced performance.

We also found that the low content of Ru can significantly boost HER property. The metallic Ru have a small kinetic barrier for H_2O dissociation into intermediate OH_{ads} and H_{ads}, which boost the initial Volmer process for HER.[54,55] Meanwhile, the electron density of Ru nanocrystals could be tuned as electron transfer from Ru to Cu after the incorporation of Ru nanocrystals into the Cu matrix, which are supposed to optimize the adsorption/desorption of intermediates of OH_{ads} and H_{ads} [56,57]. Thus, the metallic heterostructures embracing Ru and Cu nanocrystals are proposed to accelerate dissociation process, and facilitate the adsorption and desorption of OH_{ads} and H_{ads} during HER. The remarkable synergistic effect between optimizing adsorption of hydrogen and accelerating water dissociation process contributes significantly to the boosted electrocatalytic performance [57–59]. Additionally, the directly fabricated electrode on conductive support of carbon cloth also contributes to the efficient electron transfer and promote the electrolyte infiltration and accessibility of active sites du ring the catalytic reaction process [1,23,60]. As a result, Ru-Cu@CM/CC with small amount of Ru nanocrystals exhibits s excellent HER performance in alkaline medium.

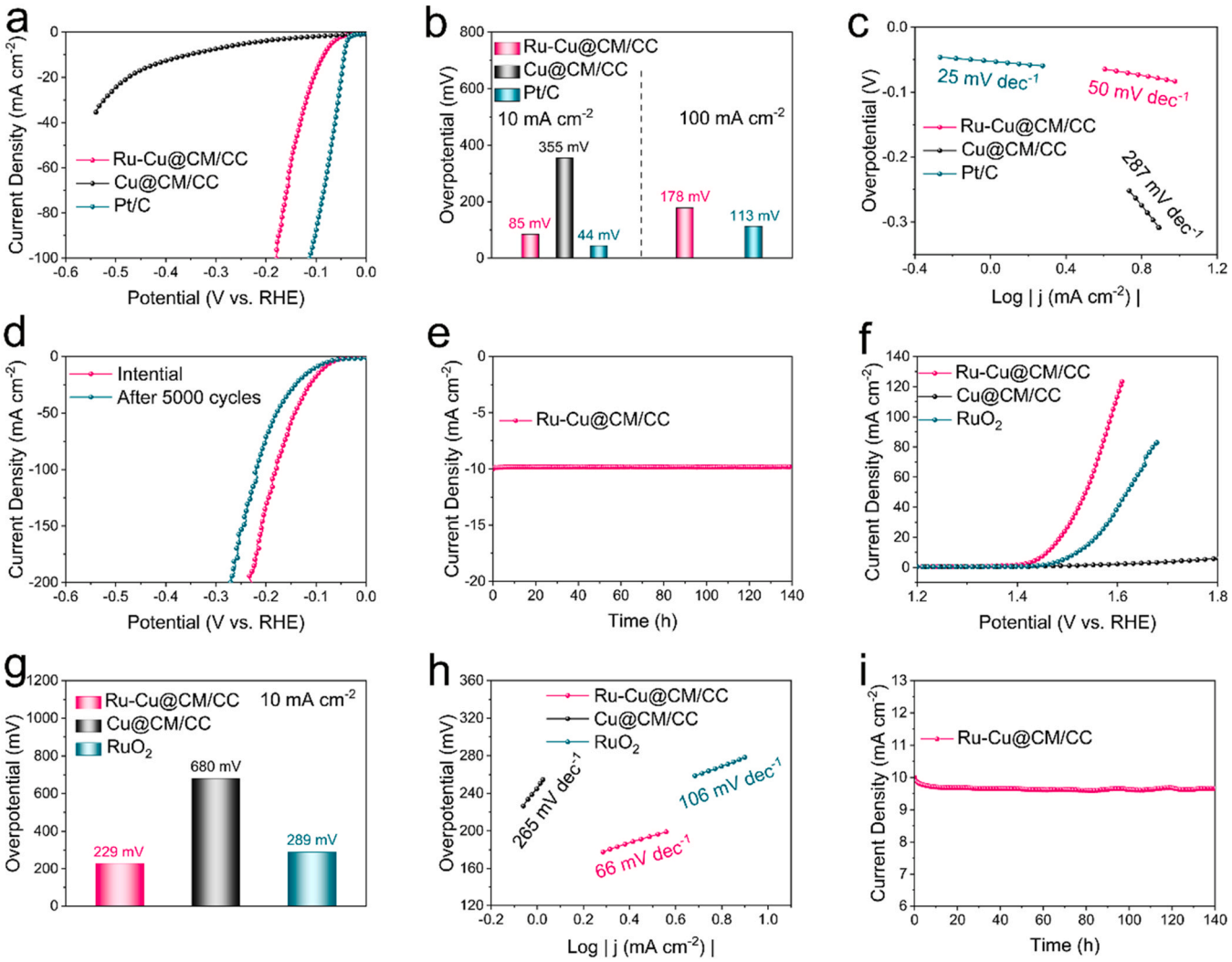

Fig. 4. (a) HER polarization curves for Ru-Cu@CM/CC, Cu@CM/CC, and Pt/C in 0.5 M H_2SO_4. (b) Comparison of overpotentials for Ru-Cu@CM/CC, Cu@CM/CC, and Pt/C at different current densities of 10 and 100 mA cm^{-2}. (c) The corresponding Tafel plots. (d) Polarization curves of Ru-Cu@CM/CC at the first cycle and after 5000 CV cycles. (e) Chronoamperometry test for Ru-Cu@CM/CC at − 85 mV. (f) OER polarization curves of Ru-Cu@CM/CC, Cu@CM/CC, and Pt/C in 0.5 M H_2SO_4. (g) Comparison of overpotentials for Ru-Cu@CM/CC, Cu@CM/CC, and RuO_2 at different current densities of 10 mA cm^{-2}. (h) The corresponding Tafel plots. (i) Chronoamperometry test for Ru-Cu@CM/CC at fixed potential of 229 mV.

The accelerated degradation tests of Ru-Cu@CM/CC for HER under the harsh electrolyte is conducted to demonstrate the potential practical applications. It is encouraged that negligible shift of polarization curves can be observed after 5000 sweeps under the scan rate of 50 mV s^{-1} (Fig. 3d). The LSV result confirms that the overpotential at j = 10 mA cm^{-2} displays a shift of only 7 mV after the accelerated durability testing. The chronoamperometry (*i-t*) test also shows that Ru-Cu@CM/CC can keep operating continuously 180 h without current density attenuation (Fig. 3e), highlighting the encouraging robustness of Ru-Cu@CM/CC. To determine the stability of as-developed Ru-Cu@CM/CC, the sample after long-term HER test were characterized by XRD, XPS and TEM. As shown in Fig. S16, the maintained metal composition and morphological structures demonstrate the robustness of the fabricated electrocatalyst. Such an excellent long-term stability feature can be attributed to the tight adherence of Cu, Ru nanocrystals on conductive substrate which is hardly peeled off from substrate.

OER activity was then evaluated in 1.0 M KOH. As shown in Fig. 3 f, the overpotential at the current density of 10 mA cm^{-2} and 20 mA cm^{-2} of Ru-Cu@CM/CC is 290 mV and 320 mV (Fig. 3 g), outperforming those for Cu@CM/CC (380 mV and 449 mV), and RuO_2 (340 mV and 408 mV). The excellent ORR performance of Ru-Cu@CM/CC is also reflected by its small Tafel slope of 78 mV dec^{-1} compared with Cu@CM/CC (206 mV dec^{-1}), and RuO_2 (87 mV dec^{-1} Fig. 3 h). As shown in Fig. 3i, Ru-Cu@CM/CC displays a remarkable long-term durability with no distinct current density deterioration under operation for 120 h at a constant overpotential of 260 mV. We emphasize that the Ru-Cu@CM/CC exhibits satisfactory morphology and metal species stability, as shown in Fig. S17. The satisfactory OER performance of Ru-Cu@CM/CC is thus reasonably attributed to the existent of abundant Ru nanocrystals, the strong interaction between Cu and Ru metallic heterostructures and conductive substrate.[47].

The HER performance is also evaluated under acid solution of 0.5 M H_2SO_4. Fig. 4a displays the LSV polarization of HER for Ru-Cu@CM/CC, Cu@CM/CC, and Pt/C. The overpotentials for provoking j = 10 mA cm^{-2} are 85 mV, 44 mV, and 355 mV, respectively (Fig. 4b). Ru-Cu@CM/CC displays an overpotential of 178 mV to attain j = 100 mA cm^{-2}, which is comparable to that of Pt/C (113 mV) and implies the exceptional activity of Ru-Cu@CM/CC. As displayed in Fig. 4c, Ru-Cu@CM/CC shows a small Tafel slope for 50 mV dec^{-1}, elucidating the decent HER kinetic in Ru-Cu@CM/CC. Next, continuous CV scanning cycles were performed with the scan rate of 50 mV s^{-1} to evaluate the stability of as-developed catalyst. As

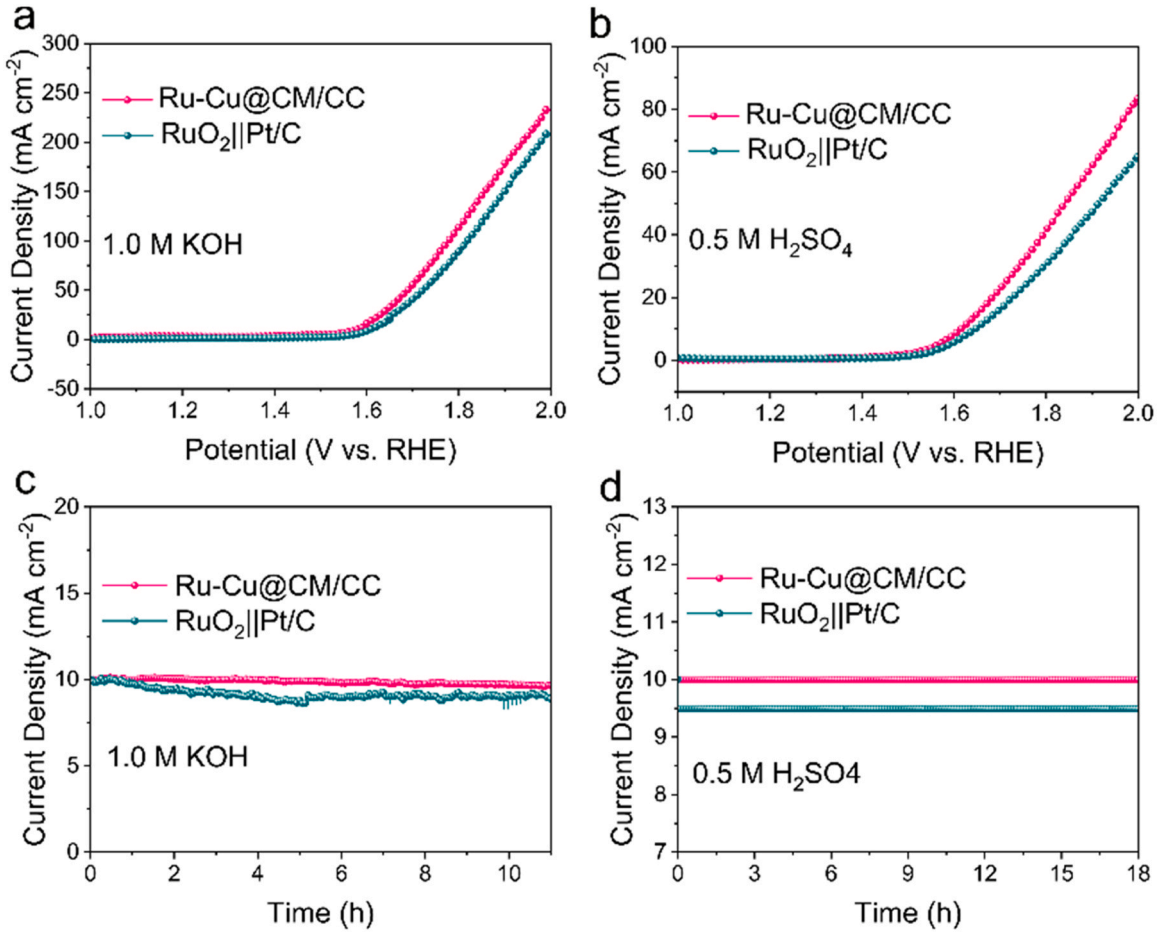

Fig. 5. LSV polarization plots of overall water splitting using Ru-Cu@CM/CC, and Pt/C + RuO_2 for both electrode catalysts respectively in (a) 1.0 M KOH, and (b) 0.5 M H_2SO_4. Chronoamperometry curves of continuous water electrolysis of Ru-Cu@CM/CC and Pt/C + RuO_2 based two electrode electrolyzer respectively at 1.57 V and 1.60 V in (c) 1.0 M KOH and (d) 0.5 M H_2SO_4.

shown in Fig. 4d, negligible difference of LSV plots could be observed after 5000 cycles testing. The current density-time responses at the potential of 85 mV with no obvious attenuation of current density after 140 h continuous working (Fig. 4e). XRD pattern and TEM image of Ru-Cu@CM/CC after HER stability test under acid condition behave the well-maintained crystal structure and morphology (Fig. S18), confirming the robustness of Ru-Cu@CM/CC.

Impressively, Ru-Cu@CM/CC also shows excellent OER performance in harsh acid solution, which meets the requirement of practical polymer electrolyte membrane water electrolyzer. Fig. 4 f displays the electrocatalytic LSV curves of OER for Ru-Cu@CM/CC, Cu@CM/CC, and RuO_2 benchmark in 0.5 M H_2SO_4. A sharp current density increase is observed for Ru-Cu@CM/CC at an onset potential of 1.42 V. For Ru-Cu@CM/CC, the overpotential are found to be 229 mV, which are much lower than RuO_2 (289 mV, and 680 mV), for obtaining the current density of 10 mA cm^{-2} (Fig. 4 g) in 0.5 M H_2SO_4 solution. Cu@CM/CC has nearly zero electrocatalytic OER performances under acid conditions when compared with Ru-Cu@CM/CC, suggesting the key role in generating excellent OER performance. It is also noteworthy that Ru-Cu@CM/CC delivers a Tafel slope of 66 mV dec^{-1}, which exceeds commercial RuO_2 (106 mV dec^{-1}) and Ru free Cu@CM/CC (265 mV dec^{-1}), indicating the remarkably improved reaction kinetics for Ru-Cu@CM/CC (Fig. 4 h). Ru doping can boost the H_2O dissociation and optimize the binding energy with intermediates, and stimulate OER activity.[61] Fig. 4i displays the chronoamperometry response of best performing Ru-Cu@CM/CC at the constant OER overpotential of 229 mV, which shows a faint current density attenuation throughout the continuous operation for 140 h. The OER polarization plots of Ru-Cu@CM/CC before and after 10,000 cyclic voltammetry (CV) cycle tests in 0.5 M H_2SO_4 solution were shown in Fig. S19. The polarization curve of Ru-Cu@CM/CC displays a slightly positive shift after OER stability test, indicating the satisfactory stability of Ru-Cu@CM/CC. In addition, Ru-Cu@CM/CC after cyclic stability test in 0.5 M H_2SO_4 solution was characterized using XRD, XPS analysis and TEM techniques. The XRD pattern (Fig. S20) is analogous to Ru-Cu@CM/CC before cyclic stability test, indicating no large crystals formed during OER. Cu 2p and Ru 3p XPS spectra reveal positive shifts of characteristic peaks, demonstrating that Cu and Ru were oxidized during OER (Fig. S21). This is in good accordance with the fact that the metals will be converted to the corresponding metal (hydro)oxide during OER. Notably, TEM images of Ru-Cu@CM/CC after OER cyclic stability test in Fig. S22 reveal the retained morphology structure, in which the nanocrystals were well-distributed on carbon support. These results suggest that Ru-Cu@CM/CC with high stability for OER is primarily due to the robustness of morphological structure.

To signify the advantages of the specific carbon matrix supported heterostructures obtained using Joule heating strategy, the catalytic activities of Ru@Cu-MOFs/CC were evaluated and compared to Ru-Cu@CM/CC. The HER and OER performance of Ru-Cu@CM/CC and Ru@Cu-MOFs/CC in various electrolytes were shown in Fig. S23. As illustrated, Ru-Cu@CM/CC shows better HER activities with smaller overpotentials than Ru@Cu-MOFs/CC. Besides, OER polarization curves for both samples show that Ru-Cu@CM/CC exhibits better OER activity than Ru@Cu-MOFs/CC. The above results demonstrate excellent electrocatalytic activity for Ru-Cu@CM/CC, and highlight

the effectiveness of Joule heating strategy in synthesizing catalytic-active electrocatalysts. Specifically, the heterostructures are capable to modulate the adsorption and desorption of intermediates, and the ultrafine nanoparticles renders significantly amount of exposed active sites. Thus, the accelerated reaction kinetics contribute to the enhanced electrocatalytic activity. Furthermore, the carbon matrix could alleviate the agglomeration of these nanoparticle and metallic heterostructures, which contribute to the robustness of electrocatalyst and remarkable stability of performance.

The performance of as-developed catalyst in neutral solution is also an important indicator, so HER and OER was tested in the neutral solution. As exhibited, HER LSV curves reveal that Ru-Cu@CM/CC possesses small overpotential of 34 mV in 1.0 M PBS neutral electrolyte at the current density of 10 mA cm^{-2}, which is 69 and 295 mV lower than Cu@CM/CC and Pt/C, respectively (Fig. S24). Remarkably, Ru-Cu@CM/CC also displays excellent long-term durability which can operate stably for 27 h in neutral electrolyte (Fig. S25). In compare with Cu@CM/CC and RuO_2, Ru-Cu@CM/CC exhibits an obvious enhancement of OER, and the overpotential to reach 10 mA cm^{-2} is only 360 mV in neutral electrolyte (Fig. S26). Clearly, Ru-Cu@CM/CC exhibits better OER activity than RuO_2, mainly because of the Ru and Cu synergistic effect.

Finally, we evaluate the overall water splitting performance of the two-electrode electrolyzer with Ru-Cu@CM/CC as both anode and cathode electrocatalyst in 1.0 M KOH, 0.5 M H_2SO_4, and 1.0 M PBS neutral electrolytes. The electrolyzer using Pt/C and RuO_2 as cathode and anode electrocatalysts, respectively, was also evaluated for comparison. The polarization curve of water splitting in a two-electrode cell is displayed in Figs. 5a and 5b. Remarkably, the LSV plots verify that Ru-Cu@CM/CC requires a low voltage of only 1.57 V and 1.6 V to obtain the current density 10 mA cm^{-2} in 1.0 M KOH and 0.5 M H_2SO_4, respectively, which is 370 mV and 410 mV lower than Pt/C+RuO_2 and most of developed electrocatalysts, respectively (Table S1 and Table S2). Additionally, the chronoamperometry plots of Ru-Cu@CM/CC-based alkali and acid electrolyzers render extremely high stability with negligible activity damping after the uninterrupted electrolysis for 11 and 18 h at the potential of 1.57 V, and 1.6 V (Figs. 5c and 5d), demonstrating the high efficiency of Ru-Cu@CM/CC for water splitting behaviors. In the two-electrode cell with neutral electrolyte, Ru-Cu@CM/CC has boosted water splitting performance compared with Pt/C+RuO_2 benchmarks. Specifically, Ru-Cu@CM/CC only need a low cell voltage of 1.8 V to 10 mA cm^{-2}, which is better than Pt/C+RuO_2 benchmarks (Fig. S27). The above results highlight the great potential of the developed bifunctional electrocatalysts with ultrafine metallic heterostructures embedded in carbon matrix in the industrialized application for water electrolysis.

4. Conclusions

In summary, we have demonstrated a facile synthesis of metallic heterostructures with ultrafine Cu and Ru nanocrystals confined in carbon matrix directly coating on carbon cloth using a flash joule heating strategy. Remarkably, Ru-Cu@CM/CC delivers impressive reaction kinetics, low overpotentials and long-term stability for HER and OER in both of alkaline acidic, and neutral electrolytes. The as-developed Ru-Cu@CM/CC possesses not only ultrafine Ru and Cu metallic heterostructure active sites but also the synergistic effect of Cu and Ru, which accounts for the encouraging HER and OER performance. The strong adherence of Cu and Ru metallic heterostructures without any binders also plays important role in improving the high stability. Moreover, the electrolyzer utilized Ru-Cu@CM/CC as both anode and cathode catalysts deliver superior performance to noble metals for overall water splitting, affording low cell voltage (of 1.57 and 1.60 V) to attain 10 mA cm^{-2} and durability in alkaline and acidic media.

CRediT authorship contribution statement

Ping Li: Investigation, Visualization, Data curation. **Wenjie Wei:** Data curation. **Jin Li**: Data curation. **Yanru Liu**: Data curation. **Kaicai Fan**: Visualization. **Lingbo Zong:** Conceptualization, Investigation, Visualization, Formal analysis, Writing – review & editing, Funding acquisition. **Lei Wang**: Visualization.

Data Availability

Data will be made available on request.

Declaration of Competing Interest

The authors declare that they have no known competing financial interests or personal relationships that could have appeared to influence the work reported in this paper.

Acknowledgements

This work was supported financially by the National Natural Science Foundation of China, China (Grant No. 52172208), and the 111 Project of China (Grant No. D20017).

Appendix A. Supporting information

Supplementary data associated with this article can be found in the online version at doi:10.1016/j.jallcom.2023.169630.

References

[1] M. Qu, Y. Jiang, M. Yang, S. Liu, Q. Guo, W. Shen, Regulating electron density of NiFe-P nanosheets electrocatalysts by a trifle of Ru for high-efficient overall water splitting, Appl. Catal. B Environ. 263 (2020) 118324–118363.
[2] X. Zhang, M. Gao, L. Qiu, J. Sheng, W. Yang, Y. Yu, Sulfur vacancies-induced "Electron Bridge" in Ni_4Mo/Sv-$Zn_xCd_{1-x}S$ regulates electron transfer for efficient H_2-releasing photocatalysis, J. Energy Chem. (2023) 64–71.
[3] X. Zhang, C. Zhu, L. Qiu, M. Gao, F. Tian, Y. Liu, W. Yang, Y. Yu, Concentrating photoelectrons on sulfur sites of $Zn_xCd_{1-x}S$ to active H-OH bond of absorbed water boosts photocatalytic hydrogen generation, Surf. Interfaces 34 (2022) 102312–102318.
[4] M. Gao, F. Tian, Z. Guo, X. Zhang, Z. Li, J. Zhou, X. Zhou, Y. Yu, W. Yang, Mutual-modification effect in adjacent Pt nanoparticles and single atoms with sub-nanometer inter-site distances to boost photocatalytic hydrogen evolution, Chem. Eng. J. 446 (2022) 137127–137137.
[5] H. Yao, S. Wang, Y. Cao, High-performance bifunctional electrocatalysts of CoFe-LDH/$NiCo_2O_4$ heterostructure supported on nickel foam for effective overall water splitting, J. Alloy. Compd. 926 (2022) 166846–166854.
[6] M. Chen, D. Liu, B. Zi, Y. Chen, D. Liu, X. Du, F. Li, P. Zhou, Y. Ke, J. Li, Remarkable synergistic effect in cobalt-iron nitride/alloy nanosheets for robust electrochemical water splitting, J. Energy Chem. 65 (2022) 405–414.263.
[7] C. Tan, F. Wang, K. Lv, Y. Shi, B. Dong, L. Hao, L. Yin, X. Xu, Y. Xian, S. Agathopoulos, TiN ceramic membrane supported nitrogen-incorporating $NiCo_2$ nanowires as bifunctional electrode for overall water splitting in alkaline solution, Sep. Purif. Technol. 298 (2022) 121582–121590.
[8] F. Wang, Y. Wu, B. Dong, K. Lv, Y. Shi, N. Ke, L. Hao, L. Yin, Y. Bai, X. Xu, Robust porous WC-based self-supported ceramic electrodes for high current density hydrogen evolution reaction, Adv. Sci. 9 (2022) 2106029–2106041.
[9] S. Liu, Y. Jiang, M. Yang, M. Zhang, Q. Guo, W. Shen, R. He, M. Li, Highly conductive and metallic cobalt-nickel selenide nanorods supported on Ni foam as an efficient electrocatalyst for alkaline water splitting, Nanoscale 11 (2019) 7959–7966.
[10] Y.Z. Wang, M. Yang, Y.M. Ding, N.W. Li, L. Yu, Recent advances in complex hollow electrocatalysts for water splitting, Adv. Funct. Mater. 32 (2022) 2108681–2108699.
[11] C. Hu, L. Zhang, J. Gong, Recent progress made in the mechanism comprehension and design of electrocatalysts for alkaline water splitting, Energy Environ. Sci. 12 (2019) 2620–2645.
[12] T.L.L. Doan, D.C. Nguyen, S. Prabhakaran, D.H. Kim, D.T. Tran, N.H. Kim, J.H. Lee, Single-Atom co-decorated MoS_2 nanosheets assembled on metal nitride nanorod arrays as an efficient bifunctional electrocatalyst for pH-universal water splitting, Adv. Funct. Mater. 31 (2021) 2100233–2100247.
[13] J. Fang, X. Qian, J. Xia, Heterostructure engineering of self-supported bimetallic sulfide as an efficient bifunctional electrocatalyst for overall water splitting, J. Alloy. Compd. 22 (2022) 168339–168368.

[14] J. Zhu, E. Jiang, X. Wang, Z. Pan, X. Xu, S. Ma, P.K. Shen, L. Pan, M. Eguchi, A.K. Nanjundan, Gram-Scale production of Cu_3P-Cu_2O janus nanoparticles into nitrogen and phosphorous doped porous carbon framework as bifunctional electrocatalysts for overall water splitting, Chem. Eng. J. 427 (2022) 130946–130955.

[15] M. Wang, L. Zhang, Y. He, H. Zhu, Recent advances in transition-metal-sulfide-based bifunctional electrocatalysts for overall water splitting, J. Mater. Chem. A 9 (2021) 5320–5363.

[16] H. Zhang, A.W. Maijenburg, X. Li, S.L. Schweizer, R.B. Wehrspohn, Bifunctional heterostructured transition metal phosphides for efficient electrochemical water splitting, Adv. Funct. Mater. 30 (2020) 2003261–2003291.

[17] G. Han, M. Li, H. Liu, W. Zhang, L. He, F. Tian, Y. Liu, Y. Yu, W. Yang, S. Guo, Short-range diffusion enables general synthesis of medium-entropy alloy aerogels, Adv. Mater. 34 (2022) 2202943–2202966.

[18] X. Guo, M. Li, L. Qiu, F. Tian, L. He, S. Geng, Y. Liu, Y. Song, W. Yang, Y. Yu, Engineering electron redistribution of bimetallic phosphates with CeO_2 enables high-performance overall water splitting, Chem. Eng. J. 453 (2023) 139796–139804.

[19] Z. Chen, R. Wu, Y. Liu, Y. Ha, Y. Guo, D. Sun, M. Liu, F. Fang, Ultrafine Co nanoparticles encapsulated in carbon-nanotubes-grafted graphene sheets as advanced electrocatalysts for the hydrogen evolution reaction, Adv. Mater. 30 (2018) 1802011–1802020.

[20] L. Zong, X. Chen, S. Liu, K. Fan, S. Dou, J. Xu, X. Zhao, W. Zhang, Y. Zhang, W. Wu, Ultrafine Fe/Fe_3C decorated on Fe-N_x-C as bifunctional oxygen electrocatalysts for efficient Zn-air batteries, J. Energy Chem. 56 (2021) 72–79.

[21] M. Streckova, O. Petrus, A. Guboova, Nanoarchitectonics of binary transition metal phosphides embedded in carbon fibers as a bifunctional electrocatalysts for electrolytic water splitting, J. Alloy. Compd. 923 (2022) 1664721–1664737.

[22] Y. Lv, J.R. Gong, In situ growth of MOF-derived ultrafine molybdenum carbide nanoparticles supported on Ni foam as efficient hydrogen-evolution electrocatalysts, J. Mater. Chem. A 9 (2021) 15246–15253.

[23] X. Han, X. Wu, Y. Deng, J. Liu, J. Lu, C. Zhong, W. Hu, Electrocatalysis: Ultrafine Pt nanoparticle-decorated pyrite-type CoS_2 nanosheet arrays coated on carbon cloth as a bifunctional electrode for overall water splitting, Adv. Energy Mater. 8 (2018) 1870110-1800946.

[24] Y. Dai, P. Lu, Z. Cao, C.T. Campbell, Y. Xia, The physical chemistry and materials science behind sinter-resistant catalysts, Chem. Soc. Rev. 47 (2018) 4314–4331.

[25] W. Zong, N. Chui, Z. Tian, Y. Li, C. Yang, D. Rao, W. Wang, J. Huang, J. Wang, F. Lai, Ultrafine MoP nanoparticle splotched nitrogen-doped carbon nanosheets enabling high-performance 3D-printed potassium-ion hybrid capacitors, Adv. Sci. 8 (2021) 2004142–2004152.

[26] B. Zhu, D. Xia, R. Zou, Metal-organic frameworks and their derivatives as bifunctional electrocatalysts, Coordin, Chem. Rev. 376 (2018) 430–448.

[27] S.J. Patil, N.R. Chodankar, S.-K. Hwang, P.A. Shinde, G.S.R. Raju, K.S. Ranjith, Y.S. Huh, Y.-K. Han, Co-metal-organic framework derived $CoSe_2$@$MoSe_2$ core-shell structure on carbon cloth as an efficient bifunctional catalyst for overall water splitting, Chem. Eng. J. 429 (2022) 132379–132409.

[28] S.N. Shreyanka, J. Theerthagiri, S.J. Lee, Y. Yu, M.Y. Choi, Multiscale design of 3D metal-organic frameworks (M-BTC, M: Cu, Co, Ni) via PLAL enabling bifunctional electrocatalysts for robust overall water splitting, Chem. Eng. J. (2022) 137045–137055.

[29] Y.-N. Chen, Y. Guo, H. Cui, Z. Xie, X. Zhang, J. Wei, Z. Zhou, Bifunctional electrocatalysts of MOF-derived Co-N/C on bamboo-like MnO nanowires for high-performance liquid-and solid-state Zn-air batteries, J. Mater. Chem. A 6 (2018) 9716–9722.

[30] F. Lu, K. Fan, L. Cui, B. Li, Y. Yang, L. Zong, L. Wang, Engineering FeN_4 active sites onto nitrogen-rich carbon with tubular channels for enhanced oxygen reduction reaction performance, Appl. Catal. B Environ. 313 (2022) 121464–121474.

[31] L. Cui, K. Fan, L. Zong, F. Lu, M. Zhou, B. Li, L. Zhang, L. Feng, X. Li, Y. Chen, Sol-gel pore-sealing strategy imparts tailored electronic structure to the atomically dispersed Ru sites for efficient oxygen reduction reaction, Energy Stor, Mater 44 (2022) 469–476.

[32] L. Zong, K. Fan, W. Wu, L. Cui, L. Zhang, B. Johannessen, D. Qi, H. Yin, Y. Wang, P. Liu, Anchoring single copper atoms to microporous carbon spheres as high-performance electrocatalyst for oxygen reduction reaction, Adv. Funct. Mater. 31 (2021) 2104864–2104874.

[33] I.T. McCrum, M. Koper, The role of adsorbed hydroxide in hydrogen evolution reaction kinetics on modified platinum, Nat. Energy 5 (2020) 891–899.

[34] S. Yuan, M. Xia, Z. Liu, K. Wang, L. Xiang, G. Huang, J. Zhang, N. Li, Dual synergistic effects between Co and Mo_2C in Co/Mo_2C heterostructure for electrocatalytic overall water splitting, Chem. Eng. J. 430 (2022) 132697–132704.

[35] K.L. Zhou, Z. Wang, C.B. Han, X. Ke, C. Wang, Y. Jin, Q. Zhang, J. Liu, H. Wang, H. Yan, Platinum single-atom catalyst coupled with transition metal/metal oxide heterostructure for accelerating alkaline hydrogen evolution reaction, Nat. Commun. 12 (2021) 1–10.

[36] T. Liu, S. Zhou, J. Qi, K. Wang, L. Zheng, Q. Huang, T. Zhou, J. Zhang, Engineering nanointerface of molybdenum-based heterostructures to boost the electrocatalytic hydrogen evolution reaction, J. Energy Chem. 58 (2021) 370–376.

[37] G. Zhao, K. Rui, S.X. Dou, W. Sun, Heterostructures for electrochemical hydrogen evolution reaction: a review, Adv. Funct. Mater. 28 (2018) 1803291-180354.

[38] D.H. Kweon, M.S. Okyay, S.-J. Kim, J.-P. Jeon, H.-J. Noh, N. Park, J. Mahmood, J.-B. Baek, Ruthenium anchored on carbon nanotube electrocatalyst for hydrogen production with enhanced Faradaic efficiency, Nat. Commun. 11 (2020) 1278–1287.

[39] W. Li, Y. Liu, M. Wu, X. Feng, S.A. Redfern, Y. Shang, X. Yong, T. Feng, K. Wu, Z. Liu, Carbon-quantum-dots-loaded ruthenium nanoparticles as an efficient electrocatalyst for hydrogen production in alkaline media, Adv. Mater. 30 (2018) 1800676-180083.

[40] Q. Wu, M. Luo, J. Han, W. Peng, Y. Zhao, D. Chen, M. Peng, J. Liu, F.M. De Groot, Y. Tan, Identifying electrocatalytic sites of the nanoporous copper-ruthenium alloy for hydrogen evolution reaction in alkaline electrolyte, ACS Energy Lett. 5 (2019) 192–199.

[41] J. Zhang, Q. Zhang, X. Feng, Support and interface effects in water-splitting electrocatalysts, Adv. Mater. 31 (2019) 1808167–1808185.

[42] Y. Yao, Z. Huang, P. Xie, S.D. Lacey, R.J. Jacob, H. Xie, F. Chen, A. Nie, T. Pu, M. Rehwoldt, Carbothermal shock synthesis of high-entropy-alloy nanoparticles, Science 359 (2018) 1489–1494.

[43] Z. Wang, B. Xiao, Z. Lin, S. Shen, A. Xu, Z. Du, Y. Chen, W. Zhong, In-situ surface decoration of RuO_2 nanoparticles by laser ablation for improved oxygen evolution reaction activity in both acid and alkali solutions, J. Energy Chem. 54 (2021) 510–518.

[44] D. Liu, H. Xu, C. Wang, H. Shang, R. Yu, Y. Wang, J. Li, X. Li, Y. Du, 3D porous Ru-doped NiCo-MOF hollow nanospheres for boosting oxygen evolution reaction electrocatalysis, Inorg. Chem. 60 (2021) 5882–5889.

[45] Y.C. Tan, H.C. Zeng, Lewis basicity generated by localised charge imbalance in noble metal nanoparticle-embedded defective metal-organic frameworks, Nat. Commun. 9 (2018) 1–8.

[46] Q. Yao, B. Huang, N. Zhang, M. Sun, Q. Shao, X. Huang, Channel-rich RuCu nanosheets for pH-universal overall water splitting electrocatalysis, Angew. Chem. 131 (2019) 14121–14126.

[47] H. Cheng, M.L. Li, C.Y. Su, N. Li, Z.Q. Liu, CuCo bimetallic oxide quantum dot decorated nitrogen-doped carbon nanotubes: a high-efficiency bifunctional oxygen electrode for Zn-Air batteries, Adv. Funct. Mater. 27 (2017) 1701833–1701842.

[48] Z. Xi, J. Li, D. Su, M. Muzzio, C. Yu, Q. Li, S. Sun, Stabilizing CuPd nanoparticles via CuPd coupling to $WO_{2.72}$ nanorods in electrochemical oxidation of formic acid, J. Am. Chem. Soc. 139 (2017) 15191–15196.

[49] W. Li, Y. Zhao, Y. Liu, M. Sun, G.I. Waterhouse, B. Huang, K. Zhang, T. Zhang, S. Lu, Exploiting Ru-induced lattice strain in CoRu nanoalloys for robust bifunctional hydrogen production, Angew. Chem, Ed 133 (2021) 3327–3335.

[50] Z. Chen, Y. Xu, D. Ding, G. Song, X. Gan, H. Li, W. Wei, J. Chen, Z. Li, Z. Gong, Thermal migration towards constructing WW dual-sites for boosted alkaline hydrogen evolution reaction, Nat. Commun. 13 (2022) 1–12.

[51] W. Yang, P. Cheng, Z. Li, Y. Lin, M. Li, J. Zi, H. Shi, G. Li, Z. Lian, H. Li, Tuning the cobalt-platinum alloy regulating single-atom platinum for highly efficient hydrogen evolution reaction, Adv. Funct. Mater. 32 (2022) 2205920–2205927.

[52] F. Wang, B. Dong, J. Wang, N. Ke, C. Tan, A. Huang, Y. Wu, L. Hao, L. Yin, X. Xu, Self-supported porous heterostructure WC/WO_{3-x} ceramic electrode for hydrogen evolution reaction in acidic and alkaline media, J. Adv. Ceram. 11 (2022) 1208–1221.

[53] T. Shinagawa, A.T. Garcia-Esparza, K. Takanabe, Insight on Tafel slopes from a microkinetic analysis of aqueous electrocatalysis for energy conversion, Sci. Rep. 5 (2015) 1–21.

[54] X. Fan, C. Liu, M. Wu, B. Gao, L. Zheng, Y. Zhang, H. Zhang, Q. Gao, X. Cao, Y. Tang, Synergistic effect of dual active sites over Ru/α-MoC for accelerating alkaline hydrogen evolution reaction, Appl. Catal. B Environ. 318 (2022) 121867–121876.

[55] B. Lu, L. Guo, F. Wu, Y. Peng, J.E. Lu, T.J. Smart, N. Wang, Y.Z. Finfrock, D. Morris, P. Zhang, Ruthenium atomically dispersed in carbon outperforms platinum toward hydrogen evolution in alkaline media, Nat. Commun. 10 (2019) 1–11.

[56] Q. Wu, M. Luo, J. Han, W. Peng, Y. Zhao, D. Chen, M. Peng, J. Liu, F.M. De Groot, Y. Tan, Identifying electrocatalytic sites of the nanoporous copper-ruthenium alloy for hydrogen evolution reaction in alkaline electrolyte, ACS Energy Lett. 5 (2019) 192–199.

[57] S. Yuan, M. Xia, Z. Liu, K. Wang, L. Xiang, G. Huang, J. Zhang, N. Li, Dual synergistic effects between Co and Mo_2C in Co/Mo_2C heterostructure for electrocatalytic overall water splitting, Chem. Eng. J. 430 (2022) 132697–132704.

[58] L. Yin, X. Du, C. Di, M. Wang, K. Su, Z. Li, In-situ transformation obtained defect-rich porous hollow CuO@CoZn-LDH nanoarrays as self-supported electrode for highly efficient overall water splitting, Chem. Eng. J. 414 (2021) 128809–128818.

[59] M. Chen, D. Liu, B. Zi, Y. Chen, D. Liu, X. Du, F. Li, P. Zhou, Y. Ke, J. Li, Remarkable synergistic effect in cobalt-iron nitride/alloy nanosheets for robust electrochemical water splitting, J. Energy Chem. 65 (2022) 405–414.

[60] X. Bai, Q.Q. Pang, X. Du, S.-S. Yi, S. Zhang, J. Qian, X.-Z. Yue, Z.-Y. Liu, Integrating RuNi alloy in S-doped defective carbon for efficient hydrogen evolution in both acidic and alkaline media, Chem. Eng. J. 417 (2021) 129319–129327.

[61] Z. Liu, M. Zha, Q. Wang, G. Hu, L. Feng, Overall water-splitting reaction efficiently catalyzed by a novel bi-functional $RuNi_3N$-Ni electrode, Chem. Comm. 56 (2020) 2352–2355.